processes

MDPI

Article

Liquid-Film Breakup and Viscosity-Dominated Transition from Hollow-Cone to Spiral-Blade Morphology in a Pressure-Swirl Nozzle

Longjie Yu [1], Wenjie Zhou [2], Jianlong Jin [1], Qunxing Huang [1] and Yiming Hu [3,*]

[1] State Key Laboratory of Clean Energy Utilization, Institute for Thermal Power Engineering, Zhejiang University, Hangzhou 310027, China; yulj@zju.edu.cn (L.Y.); 12327048@zju.edu.cn (J.J.); hqx@zju.edu.cn (Q.H.)
[2] School of Energy and Power Engineering, Jiangsu University, Zhenjiang 212013, China; zhouwenjiezwj@ujs.edu.cn
[3] Tongxiang Taiaisi Environmental Protection Energy Co., Ltd., Tongxiang 314500, China
* Correspondence: huym@wzgroup.cn

Abstract

Efficient atomization of liquid fuels over a broad range of physical properties is important for practical utilization. However, the response of pressure-swirl atomization to substantial variations in liquid viscosity remains insufficiently understood, particularly the transition from a hollow-cone atomization to a degraded atomization regime. A volume-of-fluid numerical method is employed to investigate liquid-film formation and primary breakup in a pressure-swirl nozzle over a range of viscosities and surface tensions of waste-derived pyrolysis oils in this study. The results show that increasing viscosity substantially alters the liquid-film morphology, cone angle, and primary breakup behavior. At high Reynolds numbers, a hollow-cone liquid film develops and undergoes interfacial destabilization and breakup. As the Reynolds number decreases, the hollow-cone morphology is replaced by a spiral-blade morphology. The high-viscosity condition is accompanied by substantially weakened internal swirl and circumferential mixing, allowing the liquid streams originating from individual tangential slots to retain distinct spiral paths. Consequently, centrifugal expansion is suppressed and continuous liquid persists in the central region. These results clarify the flow characteristics associated with the viscosity-dominated transition from hollow-cone to spiral-blade atomization and provide insight into the pressure-swirl atomization of liquids with a broad range of viscosities.

Keywords: liquid film fragmentation; swirl nozzle; pyrolysis oil; primary breakup

Check for updates

Academic Editor: Krzysztof Rogowski

Received: 2 September 2026
Revised: 8 October 2026
Accepted: 22 October 2026
Published: 5 November 2026

Copyright: © 2026 by the authors. Licensee MDPI, Basel, Switzerland. This article is an open access article distributed under the terms and conditions of the Creative Commons Attribution (CC BY) license.

1. Introduction

Waste-derived pyrolysis oils have attracted increasing attention as alternative liquid fuels because of the potential to partially substitute conventional petroleum-derived fuels [1–3]. Atomization is the process by which a continuous liquid phase disintegrates into smaller liquid structures and droplets under the action of aerodynamic forces and interfacial instabilities. Effective atomization is essential for the practical utilization of such fuels because it increases the gas–liquid interfacial area and promotes fuel–air mixing, thereby facilitating subsequent evaporation and combustion.

Pressure-swirl nozzles are widely used among pressure atomizers, causing the swirling flow to further enhance the atomization process. The atomization of swirl nozzles is primarily driven by the high-speed rotation. Strong internal swirling motion converts the

discharged liquid into a thin conical film, which then destabilizes and undergoes primary breakup. Ma et al. [4] found the increase in air flow rate in swirl nozzle changes flow field from a columnar to a funnel-shaped structure, enhancing the fragmentation effect. Liu et al. [5] identified three distinct breakup regimes, including rim, perforation and wave disintegration modes, occurring with the increase in Reynolds number (Re). Martino et al. [6] observed that the hollow-cone spray transitions from a conical pattern to a jet with a decrease in Re and Ohnesorge numbers (Oh) for Newtonian and non-Newtonian fluids. Yan et al. [7] proposed a compact pressure-swirl nozzle integrating tangential inlet flow channel and swirl chamber. Zheng et al. [8] studied the influence of eccentricity distance of the vortex channel on spray parameters in pressure-swirl nozzles. Liu et al. [9] designed various swirl nozzles with geometric parameters and found that the inlet and outlet diameters, inlet direction, swirl chamber diameter, and swirl chamber height affect the atomization performance. Xie et al. [10] established a nonlinear functional relationship between the variables, such as swirl chamber diameter, length, circulation area ratio, and swirl core angle by the BP method—and the swirl number, as well as the atomization effectiveness. Zhang et al. [11] obtained the optimal values for the influence of the swirl section diameter, contraction section angle, straight section diameter, and expansion section angle on the spray cone angle and liquid-film thickness. Yan et al. [12] replaced the helical flow guide groove and increased the staggered angle, resulting in an increased atomization angle and a reduced Sauter Mean Diameter (SMD).

The numerical approach constitutes a vital branch of atomization research, enabling high-fidelity analysis of underlying mechanisms that are challenging to capture experimentally. Sun et al. [13] employed a direct seamless coupling approach combining the volume-of-fluid method with Lagrangian particle tracking. The simulations revealed that instabilities develop on the conical liquid-film, leading to the formation of perforations, the detachment of filamentary structures, and the breaking up into larger droplets. Shrestha et al. [14] proposed a nasal spray atomizer volume model to study primary spray and revealed the early pre-stable and stable phases of spray plume development. Numerical atomization studies commonly employ Reynolds-averaged Navier–Stokes (RANS) [15] or large-eddy simulation (LES) approaches, whereas direct numerical simulation (DNS) remains relatively limited because of its substantially higher computational cost [16]. Liu et al. [17] used a VOF–LES framework to study disturbed liquid-jet breakup and revealed the effects of disturbance amplitude and frequency on surface-wave and ligament development. Many researchers have focused on the combination of liquid-film morphology, liquid film fragmentation mechanism, and atomization characteristics. To avoid computational cost associated with unnecessary atomization features, Dekterev et al. [18] conducted a steady-state nozzle flow simulation using a coarse grid and large time steps, followed by spatiotemporal refinement at the gas–liquid interface and initial atomization zone. To gain deeper insights into the transient characteristics of the nozzle flow field, Vashahi et al. [19] employed orthogonal decomposition to spatially visualize the vortex core inside the nozzle, thereby identifying distinct flow structures associated with specific frequencies.

The physical properties of liquid fuels play a fundamental role in pressure-swirl atomization by altering inertial, viscous, and surface-tension forces that govern internal swirling flow, air core, and the liquid film. In particular, increasing liquid viscosity enhances viscous dissipation and suppresses interfacial deformation, thereby weakening the development of the swirling liquid-film. Chung et al. [20] demonstrated that liquid viscosity and surface tension substantially influence liquid-film disintegration in simplex pressure-swirl atomizers. Liu et al. [9] proposed that temperature can substantially alter spray characteristics, because fuel viscosity is strongly temperature-dependent. Rezaei et al. [21] found that decreasing the temperature of Jet A-1 fuel increased its viscosity, resulting in a smaller spray

cone angle and substantially longer primary and secondary breakup lengths. Similar trends were reported by Rostami [22] for heavy fuel oil, which exhibited a thicker liquid film, longer breakup length and smaller spray angle than the lower-viscosity diesel fuel. More importantly, liquid properties play a critical role in determining the spray morphology [23]. Ma et al. [24] investigated the atomization characteristics of diesel swirl liquid-film breakup across various regimes, including cylindrical jetting, twisted film, open vortex, complete vortex and fully developed modes. Yue et al. [25] demonstrated that increasing liquid viscosity progressively contracts the air core and suppresses interfacial disturbances, eventually causing the hollow-cone liquid film to degenerate into a solid cylindrical jet. However, the detailed pathway by which a conventional hollow-cone liquid film loses its circumferential continuity remains unclear under strong viscous effects.

The present study focuses on the response of pressure-swirl atomization over a broad range of liquid viscosities representative of waste-derived pyrolysis oils. A three-dimensional VOF model is employed to resolve the internal swirling flow, air-core development, liquid-film formation, and primary breakup. Particular attention is paid to the transition from the conventional hollow-cone liquid film to the spiral-blade morphology at high viscosities.

2. Research Methods

2.1. The Geometry of Pressure-Swirl Nozzle

Figure 1 shows the schematic diagram and flow region of the pressure-swirl nozzle in this study. The configuration in which tangential slots are connected to a conical swirl chamber is widely used [6,14]. The fuel is directed through the tangential slots into the conical swirl chamber, converting pressure energy into rotational kinetic energy. The fluid angular momentum is conserved, as the tangential velocity multiplied by the radial distance ideally remains constant. As the fluid moves radially inward, the tangential velocity increases, leading to a larger centrifugal force. Consequently, the strongest centrifugal force occurs near the center, which effectively promotes liquid centrifuging. The centrifugal force overcomes surface tension, causing the film to accelerate outward and form a hollow-cone film. The hydrodynamic instabilities of cone film are triggered due to aerodynamic shear force, leading to liquid-film fragmentation into fine spray.

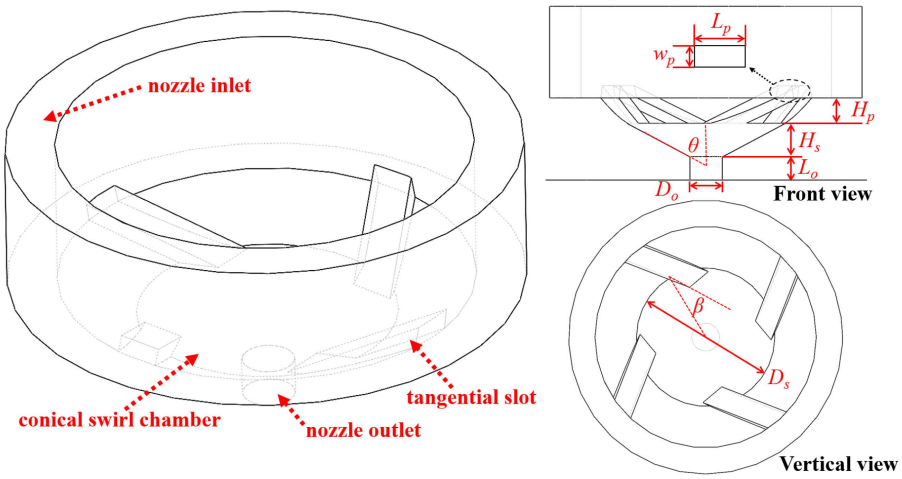


Figure 1. Schematic diagram and flow region of pressure-swirl nozzle.

The geometric sizes of the nozzle are as follows: The nozzle outlet diameter (Do) is 1 mm and the outlet length (Lo) is 0.74 mm. The number of tangential slots (N) is 4 with the rectangular inlet having a width (wp) of 0.4 mm and a length (Lp) of 0.8 mm. The height of the tangential slot (Hp) is 0.85 mm and the tangential angle (β) of the tangential

slots is 32.4°. The conical swirl chamber diameter (Ds) is 5 mm. The conical swirl chamber height (Hs) is 1.06 mm. The conical swirl chamber cone angle (θ) is 62°.

2.2. Physical Properties and Operating Cases

The pyrolysis oil is separated from the pyrolysis products of waste polymeric materials. As illustrated in Figure 2, the granulated waste rubber is typically pyrolyzed in an oxygen-deficient environment, producing the volatilization of a mixture of pyrolysis oil and gas, which requires condensation to isolate the oil phase. By controlling the production process, pyrolysis oil is separated into heavy and light fractions, which have been reported to exhibit significantly different physical properties, according to reference [26].

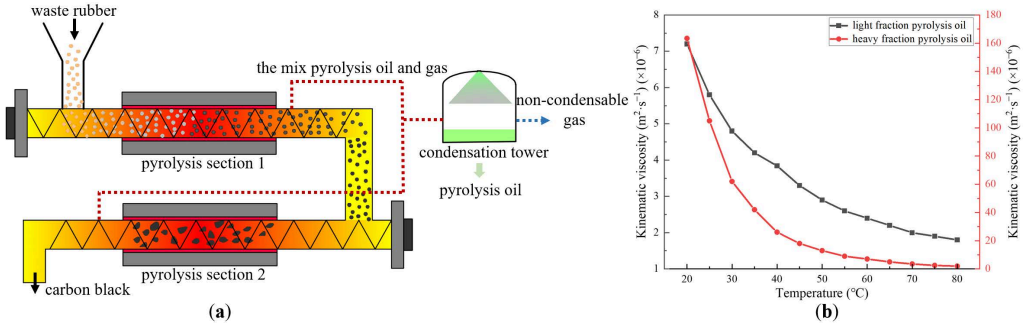


Figure 2. Waste rubber pyrolysis oil preparation and its viscosity–temperature characteristics. (**a**) Pyrolysis and condensation process, (**b**) measured kinematic viscosity.

Four representative thermophysical-property conditions were constructed from experimentally measured waste-tire pyrolysis-oil data. The physical properties adopted in the simulations are based on representative values reported for different fractions of waste rubber pyrolysis oil as shown in Table 1. The two representative fractions exhibit markedly different viscosity levels because the removal of lighter components during high-temperature condensation increases the relative contribution of heavier compounds. The viscosity measurements were performed using an NDJ-9S rotational viscometer coupled with a KDC-1WB thermostatic bath, with a stated measurement accuracy of ±2% for Newtonian liquids. Surface tension was measured using a Data Physics OCA 20 system based on the pendant-drop method. Over the measured temperature range of 15–80 °C, the kinematic viscosity of the light fraction pyrolysis oil decreased from approximately 8.1 to 1.7 $mm^2 \cdot s^{-1}$, whereas that of the heavy fraction pyrolysis oil decreased from 163.41 to 26.05 $mm^2 \cdot s^{-1}$ as the temperature increased from 20 to 40 °C. The measured densities of the light fraction and heavy fraction pyrolysis oils were 905.8 and 932.6 $kg \cdot m^{-3}$, respectively, at 20 °C, corresponding to a difference of approximately 3.0%. Therefore, a constant liquid density of 900 $kg \cdot m^{-3}$ was adopted as a controlled modeling simplification. The measured surface tensions of the two fractions were 27.36 and 31.14 $mN \cdot m^{-1}$, respectively. Accordingly, the simulations employed two representative surface-tension levels of 27.4 and 31.1 $mN \cdot m^{-1}$. The difference between these values is approximately 13.8%, which is substantially smaller than the approximately 15-fold variation in kinematic viscosity across the four simulated cases. Similar studies of pressure-swirl atomization have also reported that viscosity variations associated with temperature can be considerably larger than the corresponding variations in density and surface tension and can exert pronounced effects on internal swirling flow, liquid-sheet breakup, and spray development [21,27]. Therefore, the four cases considered here should be regarded as representative thermophysical-property conditions rather than exact reproductions of individual oil samples.

Table 1. The liquid's physical properties considered in the simulations.

Pyrolysis Oil	Case 1	Case 2	Case 3	Case 4
Kinematic viscosity ($m^2 \cdot s^{-1}$)	1.73×10^{-6}	4.51×10^{-6}	8.58×10^{-6}	25.8×10^{-6}
Dynamic viscosity ($kg \cdot m^{-1} \cdot s^{-1}$)	1.557×10^{-3}	4.059×10^{-3}	7.722×10^{-3}	2.322×10^{-2}
Surface tension (N/m)	2.74×10^{-2}	2.74×10^{-2}	3.11×10^{-2}	3.11×10^{-2}
Density (kg/m^3)	900	900	900	900
Temperature (°C)	80	32	56	40

The atomization characteristics are governed by several dimensionless numbers, which characterize the balance between inertial, viscous, and surface tension forces, as defined in Equations (1) and (2). The calculation of the dimensionless numbers primarily depends on the selection of the characteristic velocity and diameter as shown in Table 2. The liquid average velocity ($\overline{U}$) at the nozzle exit is taken as characteristic velocity. The nozzle outlet diameter (D_O) is taken as the characteristic size.

Table 2. Characteristic velocity and dimensionless parameters for different cases.

Pyrolysis Oil	Case 1	Case 2	Case 3	Case 4
Velocity ($m \cdot s^{-1}$)	21.88	21.60	21.68	23.82
Re	12,647	4789	2527	923
Oh	0.00992	0.02587	0.04613	0.13870

Reynolds number (Re) is defined as

$$\mathrm{Re} = \rho_l \overline{U} D_o / \mu_l \tag{1}$$

Ohnesorge number (Oh) is defined as

$$Oh = \mu_l / \sqrt{\rho_l \sigma D_o} \tag{2}$$

The swirl intensity is quantified by the swirl number (S), which determines the air core size and influences the liquid film. The S is evaluated at the nozzle outlet cross-section, which serves as the reference plane for characterizing the swirl intensity.

$$S = \frac{\int \rho_l U_a U_s r dA_0}{R \int \rho_l U_a^2 dA_0} \tag{3}$$

Within the present experimental measured property range, viscosity exhibits by far the largest relative variation and therefore dominates the changes in the viscosity-sensitive dimensionless *Re* and *Oh*, whereas the variations in surface tension and density are comparatively smaller. In addition, waste-tire pyrolysis oil is a compositionally complex liquid, but its major liquid fraction consists predominantly of C12–C20 hydrocarbons [28]. Because the liquid phase is dominated by relatively low-molecular-weight hydrocarbons rather than polymeric species, a Newtonian constitutive relation is adopted here as a first-order approximation for the bulk liquid.

2.3. Numerical Method

The transient gas–liquid flow and primary breakup were simulated using the volume-of-fluid (VOF) method. Air was defined as the primary phase and pyrolysis oil as the secondary phase. The two phases share a single momentum equation, while the gas–liquid interface is captured through the transport of the liquid volume fraction. Turbulence

was modeled within the Reynolds-averaged Navier–Stokes (RANS) framework using the shear-stress-transport (SST) k-ω model.

The continuity equation for the gas–liquid mixture is

$$\frac{\partial \rho}{\partial t} + \nabla \cdot (\rho \overline{u}) = 0 \tag{4}$$

The transport equation for the liquid volume fraction is

$$\frac{\partial (\alpha_l \rho_l)}{\partial t} + \nabla \cdot (\alpha_l \rho_l \overline{u}) = 0 \tag{5}$$

The mixture density and molecular viscosity are calculated as

$$\rho = \alpha_l \rho_l + (1 - \alpha_l) \rho_g \tag{6}$$

$$\mu = \alpha_l \mu_l + (1 - \alpha_l) \mu_g \tag{7}$$

The RANS momentum equation is expressed as

$$\frac{\partial (\rho \cdot \overline{u})}{\partial t} + \nabla \cdot (\rho \overline{u} \overline{u}) = -\nabla p + \nabla \cdot \left[\mu \left(\nabla \overline{u} + \nabla \overline{u}^T \right) \right] - \nabla \cdot \left(\rho \overline{u' u'} \right) + \rho \overline{g} + \overline{F}_\sigma \tag{8}$$

$F\sigma$ represents the surface-tension force per unit volume. The Reynolds stresses are closed using the Boussinesq eddy-viscosity hypothesis,

$$-\rho \overline{u_i' u_j'} = \mu_t \left(\frac{\partial \overline{u}_i}{\partial x_j} + \frac{\partial \overline{u}_j}{\partial x_i} \right) - \frac{2}{3} \rho k \delta_{ij} \tag{9}$$

The turbulent dynamic viscosity (μ_t) is obtained from the SST k-ω model. The SST formulation employs the standard k-ω model in the near-wall region and gradually blends toward a transformed k-ε formulation away from the wall, thereby retaining the near-wall accuracy of the k-ω model while reducing its sensitivity to the free-stream value of ω. The objective of the present study is therefore restricted to the resolved primary breakup, including the formation, deformation, and fragmentation of the liquid film and the transition between hollow-cone and spiral-blade atomization. The SST k-ω RANS model is used to represent the effects of unresolved turbulent fluctuations, while the gas–liquid interface structures larger than the local grid scale are directly captured by the VOF method.

Although LES/VOF offers superior resolution of transient turbulence–interface coupling and fine-scale ligament formation, its computational cost is substantially higher, particularly for simulations covering a wide range of liquid properties. Previous studies have shown that SST k-ω coupled with VOF can capture the internal swirling flow, conical liquid-film formation, and large-scale primary breakup characteristics of pressure-swirl atomizers [29,30], while direct comparisons between SST-RANS/VOF and LES/VOF indicate that LES provides an improved resolution of fine-scale atomization and droplet statistics [31]. The present simulations are intended to resolve the large-scale liquid-film formation, deformation, and primary breakup morphology, including the transition from hollow-cone to spiral-blade atomization, rather than the full turbulence spectrum, minimum droplet sizes, or fine-scale ligament statistics. The RANS SST + VOF thus represents a compromise between resolving the dominant primary breakup morphology and maintaining a feasible computational cost for the present parametric study.

2.4. Numerical Settings

All transient simulations were performed using the pressure-based solver. A pressure inlet boundary condition was imposed at the nozzle inlet with a gauge pressure of 1 MPa, while the outlet was specified as a pressure outlet with a gauge pressure of 0 Pa. The operating pressure was set to 101,325 Pa. All solid surfaces were treated as stationary no-slip walls.

Pressure–velocity coupling was achieved using the coupled algorithm. The pressure field was discretized using the PRESTO! scheme, while the momentum equation was discretized using the second-order upwind scheme. The turbulent kinetic energy and specific dissipation rate equations were discretized using the first-order upwind scheme. The VOF equation was solved using the implicit formulation, and the compressive scheme was employed for interface reconstruction. Surface tension was represented using the continuum surface force (CSF) model. A first-order implicit scheme was used for temporal discretization. An adaptive time-stepping scheme was employed, with the maximum Courant number restricted to 0.6 to improve the numerical stability of the transient gas–liquid interface calculation. Courant-controlled time stepping has been widely adopted in VOF simulations of swirling liquid-sheet breakup and pressure-swirl atomization. For example, Liu et al. [9] employed a CFL number below 1, while Shrestha et al. [14] restricted the maximum Courant number to 1. Similarly, Harizi et al. [31] adopted a time-step size of approximately 10^{-7} s to maintain CFL below 1. Compared with these reported settings, the present study adopted a more restrictive Courant-number limit of 0.6 to improve numerical stability during transient interface evolution.

2.5. Grid and Verification

The structured base mesh for the internal and external flow regions of the pressure-swirl nozzle is shown in Figure 3a, while the internal nozzle geometry is presented in Figure 3b. The external computational domain is cylindrical, with a diameter of 40 mm and an axial length of 50 mm, covering the nozzle outlet and the downstream near-field atomization region. To balance spatial resolution and computational cost, local refinement in the critical internal-flow regions was adopted at the nozzle exit and in the near-nozzle region, whereas relatively coarser cells were employed farther downstream. The initial base mesh contained approximately 2.31×10^6 cells, with a minimum cell size of approximately 23 μm near the nozzle exit before adaptive refinement. To better resolve local liquid-sheet deformation and primary breakup, a liquid-volume-fraction-based adaptive mesh refinement (AMR) strategy was employed in the transient VOF simulations. Cells satisfying the refinement criterion were locally refined, while cells meeting the coarsening criterion were coarsened, thereby concentrating computational resources in and around the evolving liquid–gas interface.

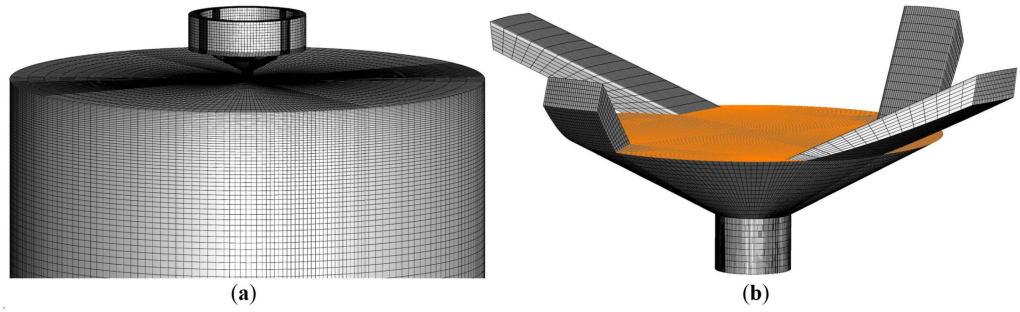


Figure 3. The grid diagram of swirl nozzle. (**a**) Structured base mesh, (**b**) internal nozzle mesh.

To examine the sensitivity of the predicted liquid-sheet morphology and major flow characteristics to interfacial mesh resolution, two configurations with maximum AMR levels of 1 and 2 were considered. Where the same base-mesh cells undergo successive isotropic refinement, the characteristic local cell width at Level 2 is approximately half that at Level 1. The comparison focuses on the outlet-averaged velocity and outlet swirl number for the representative hollow-cone Case 3. At AMR Levels 1 and 2, the outlet-averaged velocities were 22.93 and 21.68 m/s, respectively, while the corresponding swirl numbers were 0.582

and 0.614. Taking the Level 2 results as reference, the relative differences in outlet-averaged velocity and swirl number were approximately 5.77% and 5.21%, respectively. These modest variations indicate that the major outlet flow characteristics exhibit limited sensitivity to further interfacial mesh refinement. With a maximum AMR level of 2, the cell count during the quasi-steady atomization stage was approximately 3.16×10^6.

The transient liquid-film evolution predicted by the present model was qualitatively compared with experimental observations reported in the literature on pressure-swirl atomization. Van Strien et al. [32] used high-speed imaging to document the developing and fully developed stages of spray formation. The characteristic distorted-pencil, onion, and tulip morphologies during the early development of pressure-swirl sprays have also been discussed in previous studies [14,32]. The present simulation captures a similar morphological progression from an initial liquid column to an expanding conical liquid sheet, followed by liquid-sheet destabilization and breakup, as illustrated in Figure 4a. Furthermore, Yao et al. [33] experimentally investigated the transient atomization of water–glycerol mixtures using a swirl atomizer with a 1 mm outlet diameter and three tangential inlets. Under high-viscosity conditions, liquid-sheet breakup was suppressed, and a three-branched liquid-sheet structure accompanied by a rotating liquid stream was observed. Similarly, the high-viscosity case in the present study exhibits an incompletely expanded liquid sheet, consisting of four coherent spiral sheets surrounding a persistent central liquid column, as illustrated in Figure 4b. The number and arrangement of these spiral sheets are associated with the four-slot geometry of the present nozzle. The qualitative similarities between the present numerical observations and previously reported experimental phenomena provide support for the physical plausibility of the simulated liquid-film evolution and morphology transition.

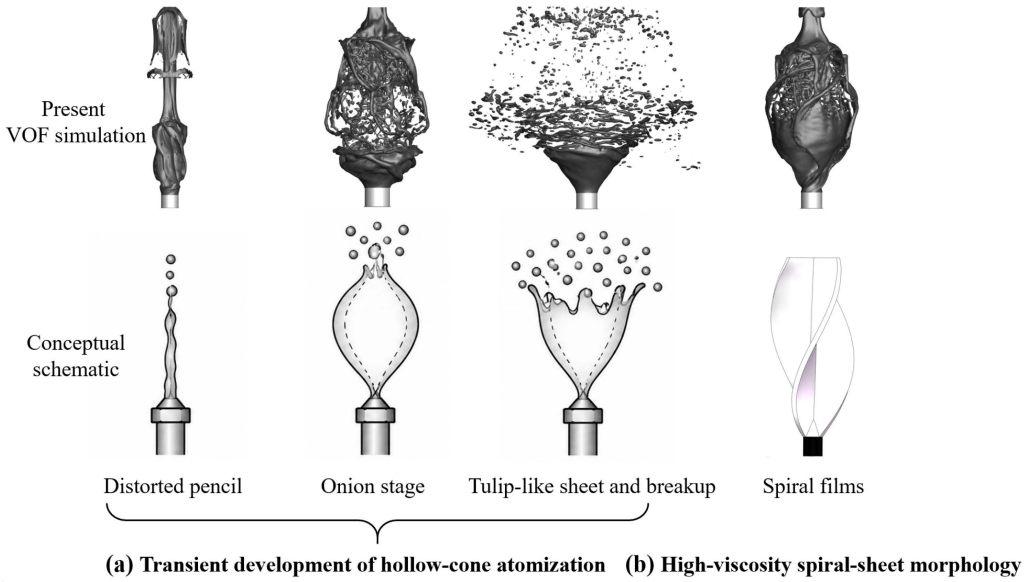


Figure 4. Qualitative comparison of liquid-film evolution and morphology transition. (**a**) Transient development, (**b**) high-viscosity morphology.

3. Results

3.1. Liquid-Film Transition from Hollow Cone to Spiral Blade

Figure 5 presents the three-dimensional liquid-film morphology and cross-section velocity contours under different *Re*. As shown in Figure 5a–c, inertial and centrifugal forces dominate under high *Re*, generating a hollow-cone liquid film. The film subsequently undergoes breakup via interfacial instability, disintegrating into dispersed liquid fragments.

In contrast, as shown in Figure 5d, the liquid film fails to fully expand, forming a spiral-blade jet linked to liquid column via residual liquid bridges. The marked reduction in swirl number and tangential velocity indicates a substantial attenuation of rotational motion under the high-viscosity condition. The transition demonstrates that high viscosity suppresses interfacial instabilities and delays primary breakup and deteriorates overall atomization quality.

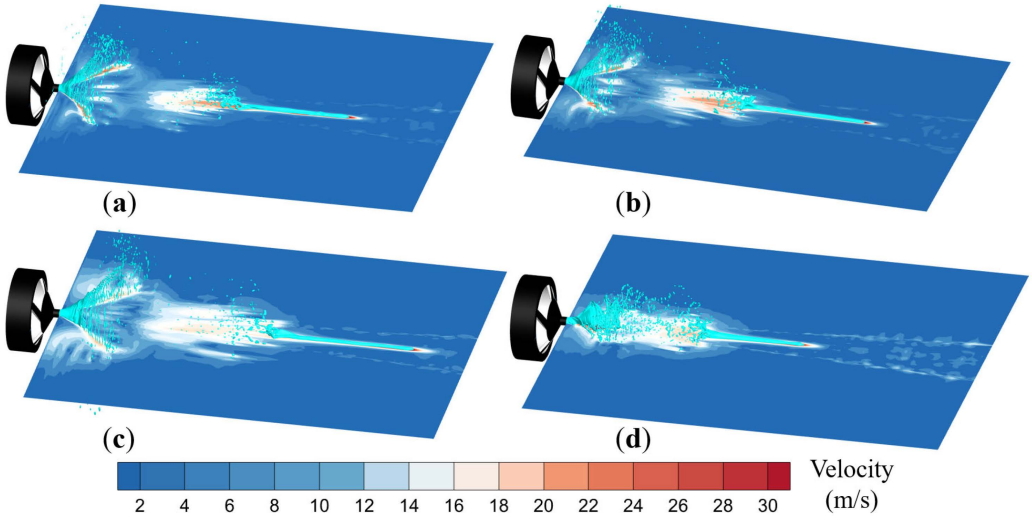


Figure 5. The three-dimensional liquid-film morphology and cross-section velocity contours under different *Re*. (**a**) *Re* = 12,647, (**b**) *Re* = 4789, (**c**) *Re* = 2527, (**d**) *Re* = 923.

Figure 6 shows the three-dimensional liquid-film prior to complete breakup under different *Re*. As shown in Figure 6a–c, the uniform swirling flow is induced by the conical swirl chamber from the bottom-view. The oil accelerates through the four tangential slots into the conical swirl chamber, resulting in four spiral wrinkles along the conical liquid film, as seen in Figure 6a,b. The hollow-cone morphology is retained in Case 3 at *Re* = 2527, *Oh* = 0.04613, and *S* = 0.614, whereas Case 4 exhibits a spiral-blade morphology, as shown in Figure 6d at *Re* = 923, *Oh* = 0.13870, and *S* = 0.321. It is indicated that the morphology transition is bracketed between these two operating states for the present nozzle configuration. The fluid near the conical swirl chamber wall maintains a high tangential velocity due to the continuous momentum transfer from the fluid ejected from the tangential slots. In contrast, the fluid in the central region experiences rapid dissipation of initial angular momentum through intense viscous internal friction, leading to a sharp drop in tangential velocity. Furthermore, the fluid streams ejected from each tangential slot exhibit weak mixing in the circumferential direction, instead maintaining their own independent liquid film trajectories, thereby forming spiral films whose number equals the number of slots. The *S* decreases from 0.617 (a), 0.637 (b) and 0.614 (c) to 0.321 (d) as viscosity increases. The decrease in *S* suppresses the centrifugal expansion of the liquid film.

Figure 7 illustrates the stable cone angle of the liquid film under different *Re*. An approximate elliptical air core forms at the nozzle exit from Figure 7a–c. The liquid film exhibits pronounced surface instabilities and strong fluctuations, producing a hollow-cone liquid film with a larger cone angle under high *Re* and low *Oh*. For Cases 1 (*Re* = 12,647) and 2 (*Re* = 4789), the measured cone angles are both approximately 79°, indicating that the liquid film expands fully under the dominance of centrifugal and inertial forces at high *Re*. For Case 3 (*Re* = 2527), the cone angle decreases slightly to about 72°. This reduction is attributed to the increased viscous dissipation, which weakens the centrifugal expansion of the liquid film. The breakup length increases with the decrease in *Re*. As shown in

Figure 7d, the air core disappears and is replaced by a continuous liquid column at the nozzle exit. Four spiral liquid-film structures develop around the central column and extend downstream while the central liquid column gradually narrows.

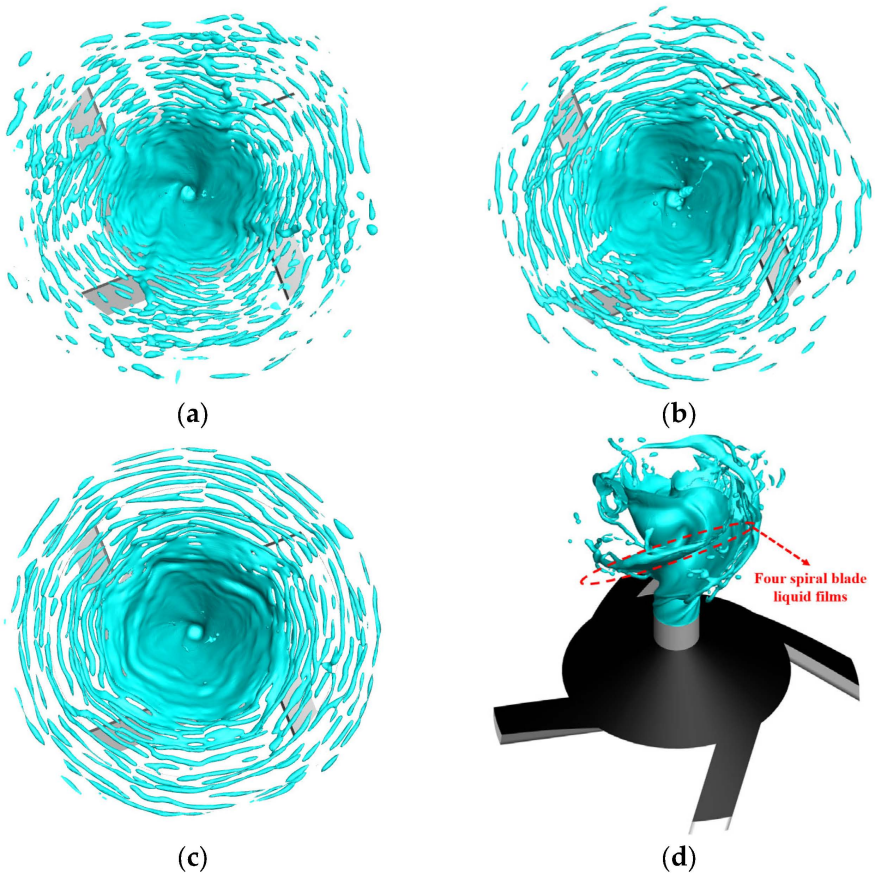


Figure 6. The three-dimensional liquid film prior to complete breakup from bottom-view under different *Re* (**a**) *Re* = 12,647, (**b**) *Re* = 4789, (**c**) *Re* = 2527, (**d**) *Re* = 923.

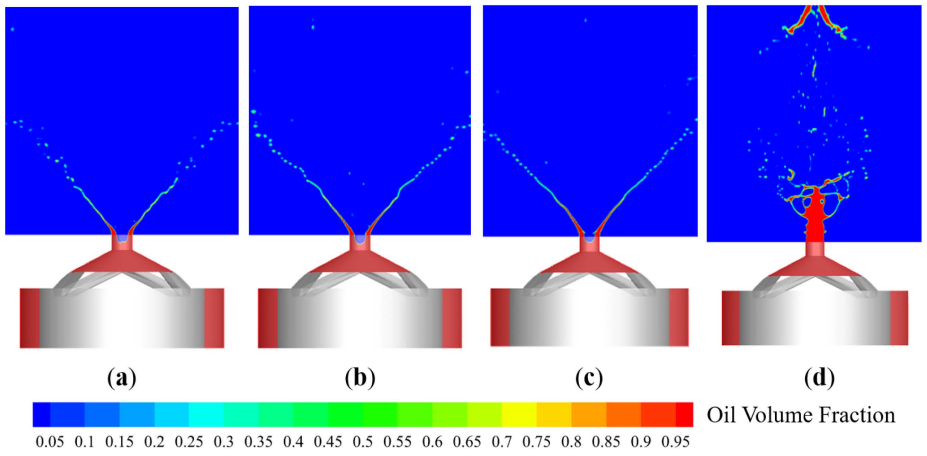


Figure 7. The stable cone angle of the liquid film under different *Re*. (**a**) *Re* = 12,647, (**b**) *Re* = 4789, (**c**) *Re* = 2527, (**d**) *Re* = 923.

3.2. Transient Evolution of Hollow-Cone and Spiral-Blade Atomization

Figure 8 presents the transient liquid film morphology and velocity of hollow-cone atomization. The atomization process can be divided into three stages, including liquid injection, liquid-film development and primary breakup. Before the establishment of stable

swirl flow in the conical swirl chamber, the injected liquid forms a straight column jet without centrifugal force, as shown in Figure 8a. As rotational momentum transfers to the tail of the liquid column, it deforms and splits into four spiral coherent films, reflecting the four tangential slots and signifying the transition from a simple jet to swirling flow. Figure 8b shows that the initial development of the cone angle occurs as the onion stage approaches breakup. The primary breakup instability is driven by the inertial and centrifugal forces supplied from upstream of the nozzle, which overcame the surface tension and viscous forces, leading to the appearance of interfacial instability on the liquid film. Consequently, as depicted in Figure 8c, localized ruptures in the thin liquid film initiate the ligaments formation. The elongated ligaments subsequently undergo capillary breakup into smaller resolved liquid fragments. The development of the conical liquid film induces the separation between the straight liquid column and the conical film, as shown in Figure 8e. At the rupture region between the conical liquid film and the straight liquid column, the thin and tearing liquid ligaments and numerous dispersed liquid fragments can be observed. Simultaneously, perforation breakup occurs on the fully developed liquid film as shown in Figure 8f.

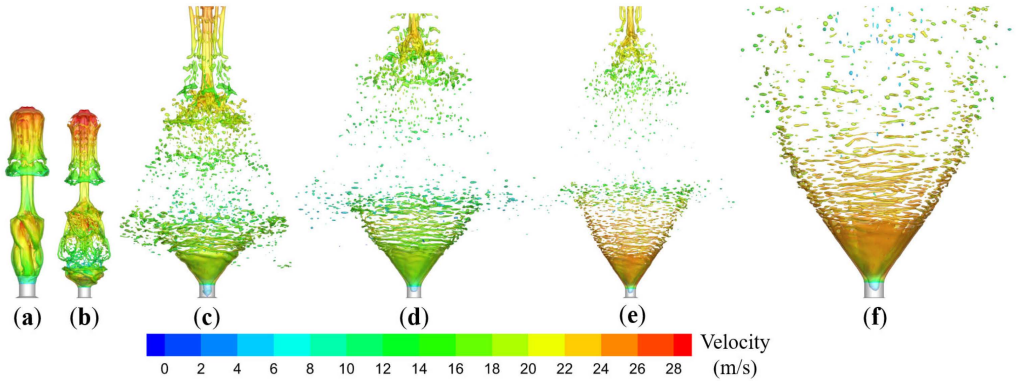


Figure 8. The transient liquid-film morphology and velocity of hollow-cone atomization. (**a**) initial liquid column, (**b**) onion stage, (**c**) ligament formation, (**d**) conical-film development, (**e**) liquid-column/film separation, (**f**) fully developed hollow-cone atomization.

Figure 9 presents the transient liquid-film morphology and velocity of spiral-blade atomization. As shown in Figure 9a, the injected liquid initially forms a straight column jet in the absence of sufficient centrifugal force. The jet tail subsequently splits into four coherent spiral films due to flow development by the four tangential slots. These films stretch into a stable elliptical rotating structure rather than undergo rapid breakup. The overall shape of the rotating liquid film at the nozzle exit evolves into a conical form with flow development, as illustrated in Figure 9b. A large number of dispersed liquid fragments are generated in the region between the rotating conical film and the straight liquid column. This phenomenon stems from the competition between the centrifugal force driving film expansion and the inertial force sustaining the jet. As depicted in Figure 9d,e, the rotating liquid film continues to develop under centrifugal force, resulting in its thinning and rupture, and stretching into ring-like liquid ligaments. As seen in Figure 9e, the centrifugal force acting on the spiral film is significantly weaker in the central region. Consequently, a continuous liquid core persists in the central region, whereas fragmentation is concentrated mainly along the peripheral spiral films, resulting in reduced radial dispersion and poorer overall atomization.

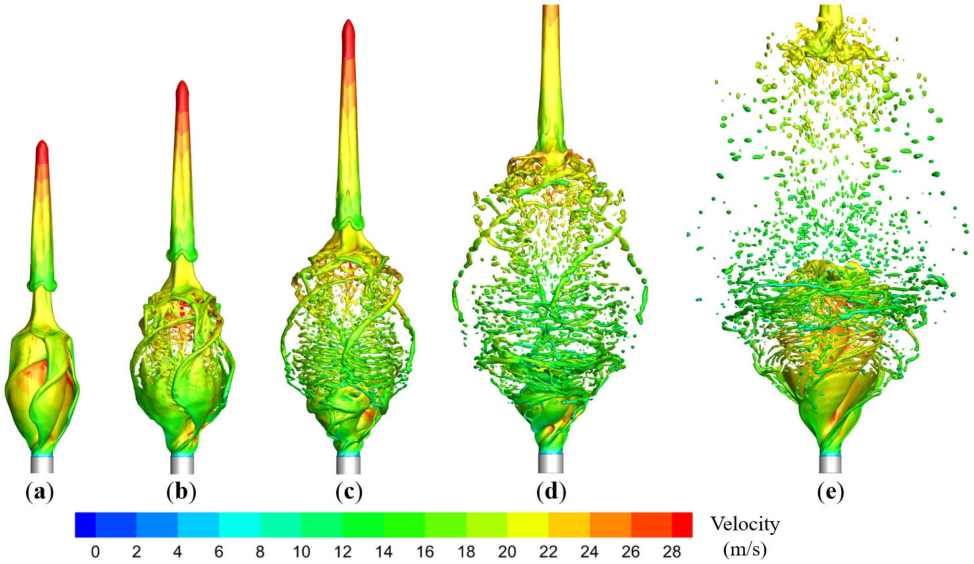


Figure 9. The transient liquid-film morphology and velocity of spiral-blade atomization. (**a**) initial liquid column, (**b**) spiral-film development, (**c**) dispersed liquid fragments, (**d**) spiral-film thinning and rupture, (**e**) developed spiral-blade atomization.

3.3. Resolved Liquid Fragmentation in Hollow-Cone and Spiral-Blade Atomization

Figure 10a,b show the center cross-section liquid film and dispersed liquid fragments' velocity contours and vectors in the hollow-cone and spiral-blade atomization. As seen in Figure 10a, the conical liquid film expands radially at a finite spray angle. The expansion of the conical spray is accompanied by a broadening of the high-velocity region, reflecting an increase in the degree of flow fragmentation. The liquid film expands radially while being deflected downward by gravity. Figure 10b illustrates the process of ligament breakup into liquid fragments. The liquid fragment velocities noticeably decrease after expansion. In contrast to conical atomization, Figure 10c shows that an outward radial vector exists only at the spiral-blade region, accompanied by significant deceleration. Figure 10d shows that the velocity vectors of the spatially rotating liquid film flow downward along the spiral direction and turn rapidly downward after breakup. The liquid fragment velocity vectors are mainly downward with little radial dispersion, leading to low spatial coverage.

Figure 11 illustrates the injection streamline, internal flow vector and axial velocity profiles at different distances (y_1, y_2, y_3) across the near-nozzle cross-section. The formation of the conical liquid film exhibits a correlation with the swirling flow within the conical swirl chamber. As shown in Figure 11a, the pyrolysis oil enters the conical swirl chamber through the tangential slots with a high initial rotational velocity. As the flow converges toward the nozzle outlet in the conical chamber, the decreasing flow radius leads to an increase in swirl velocity. It gradually mixes with the surrounding fluid, resulting in a homogenization of the rotational speed. Once the conical liquid film is expelled from the nozzle, the swirl intensity decays. The axial velocity peak emerges at $y_1 = 1$ mm for the spiral-blade liquid film from Figure 11b. The symmetric distribution is evident about the central axis for the conical liquid film. As shown in Figure 11c at $y_2 = 4$ mm, the axial velocity near the centerline decays rapidly, splitting into four distinct peaks in the spiral-blade liquid film. The maximum velocity for the spiral-blade liquid film drops to approximately 22 m/s from Figure 11d at $y_3 = 8$ mm. In contrast, the spiral-blade film generates multiple velocity peaks, reflecting the persistence of several coherent liquid films and ligaments. All figures reveal that the velocity peak of conical liquid film progressively decreases and broadens in range consistently, promoting film destabilization and atomization. The region between the two velocity peaks of the hollow-cone liquid film exhibits intermittent negative axial velocity,

indicating local reverse flow or recirculation. As the swirling motion decays downstream and the reverse-flow region weakens, the axial velocity in the central region of Case 1 eventually becomes positive.

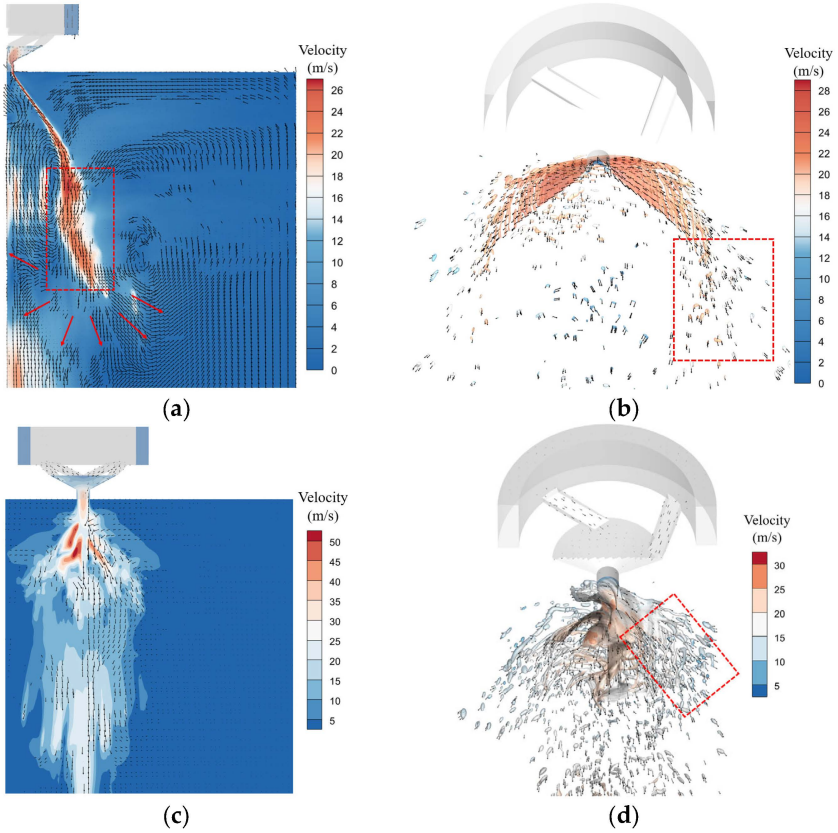


Figure 10. The center cross-section liquid film and dispersed liquid fragments' velocity contours and vectors: (**a**) hollow-cone atomization, (**b**) hollow-cone atomization, (**c**) spiral-blade atomization, (**d**) spiral-blade atomization.

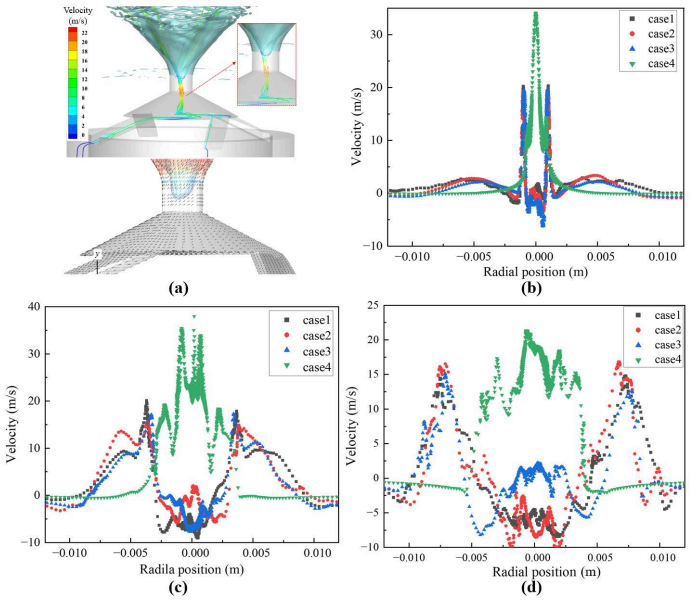


Figure 11. The injection streamline, internal flow vector and axial velocity profiles across the near-nozzle cross-section: (**a**) streamline and internal flow vector, (**b**) y_1 = 1 mm, (**c**) y_2 =4 mm, (**d**) y_3 = 8 mm.

4. Conclusions

Clarifying the atomization performance and liquid fragmentation mechanisms of waste-derived pyrolysis oils in pressure-swirl nozzles is critical for enabling the efficient utilization of alternative fuels. Based on a VOF numerical simulation method and interface-refinement method, the liquid-film fragmentation and atomization characteristics of waste-derived pyrolysis oil with a wide range of physical properties are investigated in a pressure-swirl nozzle in this study.

Variations in the physical properties of pyrolysis oil, dominated by viscosity, significantly affect the primary breakup mode, stable cone angle and liquid-film morphology. The hollow-cone liquid-film breakup is accompanied by interfacial instability, promoting liquid-film thinning, expanding the cone angle and decreasing liquid-film breakup length with the increase in *Re*. The hollow-cone liquid film degenerates into a spiral-blade shape as *Re* decreases from 12,647 to 923. At low *Re*, the circumferential mixing capability of the fluid is extremely weak. The jets discharged from each tangential slot develop independently and cannot merge into a continuous liquid film. Consequently, four spiral liquid-film structures develop around a persistent central liquid column, resulting in deteriorated atomization. Under the investigated nozzle geometry and inlet-pressure condition, the transition is associated with the variations in liquid properties, with viscosity representing the dominant property variation. The transition boundary may shift with nozzle geometry, slot configuration, injection pressure, and flow rate. For high-viscosity liquids, maintaining sufficient internal swirl and tangential momentum transfer is important for preserving a hollow-cone spray. Operational measures that reduce liquid viscosity may therefore improve atomization. This study is limited to nozzles with a specific number and geometry of tangential slots. The effects of slot geometry and operating conditions on the transition between hollow-cone and degraded atomization regimes will be investigated in future work.

Author Contributions: Conceptualization, L.Y. and Y.H.; methodology, L.Y.; software, L.Y.; validation, J.J.; formal analysis, W.Z.; investigation, Y.H.; resources, Q.H.; data curation, L.Y.; writing—original draft preparation, L.Y.; writing—review and editing, W.Z.; visualization, W.Z.; supervision, Q.H.; project administration, Q.H.; funding acquisition, Y.H. All authors have read and agreed to the published version of the manuscript.

Funding: This research was funded by the Science and Technology Department of Zhejiang Province under the Zhejiang Provincial Key Research and Development Program, grant number 2025C02207.

Data Availability Statement: The original contributions presented in this study are included in the article. Further inquiries can be directed to the corresponding authors.

Conflicts of Interest: Author Yiming Hu was employed by the company Tongxiang Taiaisi Environmental Protection Energy Co., Ltd. The remaining authors declare that the research was conducted in the absence of any commercial or financial relationships that could be construed as a potential conflict of interest.

Nomenclature

A_0	Nozzle outlet area (mm^2)
D_O	Nozzle outlet diameter (mm)
D_s	Conical swirl chamber diameter (mm)
$F\sigma$	Surface-tension force per unit volume (N/m^3)
$\overline{g}$	Gravity acceleration (m/s^2)
H_p	Tangential slot height (mm)
H_s	Conical swirl chamber height (mm)
k	Turbulent kinetic energy (m^2/s^2)

L_0	Nozzle outlet length (mm)
L_p	Rectangular inlet length (mm)
N	Number of tangential slot (dimensionless)
Oh	Ohnesorge Number (dimensionless)
p	Pressure (Pa)
r	Grid node radius (m)
R	Characteristic radius (m)
Re	Reynolds number (dimensionless)
S	Swirl number (dimensionless)
t	Time (s)
U_a	Axial velocity (m/s)
U_s	Tangential velocity (m/s)
$\overline{U}$	Mean liquid velocity at the nozzle outlet (m/s)
$\overline{u}$	Mean velocity vector (m/s)
u_i	Velocity component of i direction (m/s)
u_j	Velocity component of j direction (m/s)
w_p	Rectangular inlet width (mm)
x_i	Cartesian coordinate in the i direction (m)
x_j	Cartesian coordinate in the j direction (m)
α_l	Liquid volume fraction (dimensionless)
β	Tangential angle of the tangential slots (°)
δ_{ij}	Kronecker delta (dimensionless)
θ	Cone angle of conical swirl chamber (°)
μ	Mixture dynamic viscosity (Pa·s)
μ_g	Gas dynamic viscosity (Pa·s)
μ_l	Liquid dynamic viscosity (Pa·s)
μ_t	Turbulent dynamic viscosity (Pa·s)
ρ	Mixture density (kg/m^3)
ρ_g	Gas density (kg/m^3)
ρ_l	Density of pyrolysis oil (kg/m^3)
σ	Surface tension of gas–liquid phase (N/m)
ω	Specific dissipation rate (s^{-1})

References

1. Dai, L.; Zhou, N.; Lv, Y.; Cheng, Y.; Wang, Y.; Liu, Y.; Cobb, K.; Chen, P.; Lei, H.; Ruan, R. Pyrolysis Technology for Plastic Waste Recycling: A State-of-the-Art Review. *Prog. Energy Combust. Sci.* **2022**, *93*, 101021. [CrossRef]
2. Mahari, W.A.W.; Azwar, E.; Foong, S.Y.; Ahmed, A.; Peng, W.; Tabatabaei, M.; Aghbashlo, M.; Park, Y.-K.; Sonne, C.; Lam, S.S. Valorization of Municipal Wastes Using Co-Pyrolysis for Green Energy Production, Energy Security, and Environmental Sustainability: A Review. *Chem. Eng. J.* **2021**, *421*, 129749. [CrossRef]
3. Jahirul, M.I.; Rasul, M.G.; Schaller, D.; Khan, M.M.K.; Hasan, M.M.; Hazrat, M.A. Transport Fuel from Waste Plastics Pyrolysis—A Review on Technologies, Challenges and Opportunities. *Energy Convers. Manag.* **2022**, *258*, 115451. [CrossRef]
4. Ma, X.; Wang, S.; Li, F.; Zhang, H.; Jiang, S.; Sui, M. Effect of Air Flow Rate and Temperature on the Atomization Characteristics of Biodiesel in Internal and External Flow Fields of the Pressure Swirl Nozzle. *Energy* **2022**, *253*, 124112. [CrossRef]
5. Liu, Y.; Beji, T.; Thielens, M.; Tang, Z.; Fang, Z.; Merci, B. Numerical Analysis of a Water Mist Spray: The Importance of Various Numerical and Physical Parameters, Including the Drag Force. *Fire Saf. J.* **2022**, *127*, 103515. [CrossRef]
6. Di Martino, M.; Ahirwal, D.; Maffettone, P.L. Three-Dimensional Computational Fluid Dynamics Simulation of the Hollow-Cone Spray Process: The Stability of the Conical Liquid Sheet. *Phys. Fluids* **2021**, *33*, 063301. [CrossRef]
7. Yan, J.-D.; Zheng, L.; Chen, H.; Cheng, W.-L. Study on Spray Characteristics of a Compact Pressure Swirl Nozzle Integrating Tangential Inlet Flow Channel and Swirl Chamber. *Phys. Fluids* **2024**, *36*, 043341. [CrossRef]
8. Zheng, L.; Zhao, R.; Nian, Y.-L.; Liu, J.; Cheng, W.-L. Numerical and Experimental Study of the Effects of Tangential to Axial Velocity Ratio and Structural Parameters inside the Nozzle on Spray Characteristics. *Phys. Fluids* **2023**, *35*, 043303. [CrossRef]
9. Liu, J.; Feng, X.; Liang, H.; Zhang, W.; Hui, Y.; Xu, H.; Yang, C. Prediction of Atomization Characteristics of Pressure Swirl Nozzle with Different Structures. *Chin. J. Chem. Eng.* **2023**, *63*, 171–184. [CrossRef]
10. Xie, Y.; Ye, Y.; Yu, H.; Cheng, W.; Xie, S.; Zhao, J. Influence Law of Structural Parameters of Pressure-Swirl Nozzle on Atomization Effect Based on Multiscale Model. *Environ. Sci. Pollut. Res.* **2023**, *30*, 60129–60149. [CrossRef]
11. Zhang, T.; Chen, J.; Wan, P.; Wang, Y.; Li, R. Effects of Key Structure of Pressure Swirl Nozzle on Atomization Performance. *Int. J. Aerosp. Eng.* **2023**, *2023*, 5534452. [CrossRef]

12. Yan, J.; Wang, F.; Li, Y.; Liu, H.; Gao, Y.; Li, Z.; Li, Z. Influence of Swirl Intensity on Atomization Characteristics and Dust-Reduction Using Pressure Swirl Nozzle. *Energy Sources Part A Recovery Util. Environ. Eff.* **2025**, *47*, 10895–10915. [CrossRef]
13. Sun, Y.; Alkhedhair, A.M.; Guan, Z.; Hooman, K. Numerical and Experimental Study on the Spray Characteristics of Full-Cone Pressure Swirl Atomizers. *Energy* **2018**, *160*, 678–692. [CrossRef]
14. Shrestha, K.; Van Strien, J.; Fletcher, D.F.; Inthavong, K. Primary Spray Breakup from a Nasal Spray Atomizer Using Volume of Fluid to Discrete Phase Model. *Phys. Fluids* **2023**, *35*, 053312. [CrossRef]
15. Lin, X.; Lin, T.; Xu, G.; Chen, G.; Xu, F. Three-Dimensional Numerical Simulation of High-Speed Shear Crushing of High-Density Fluid. *Processes* **2024**, *12*, 2246. [CrossRef]
16. Li, Y.; Ries, F.; Sun, Y.; Lien, H.-P.; Nishad, K.; Sadiki, A. Direct Numerical Simulation of Atomization Characteristics of ECN Spray-G Injector: In-Nozzle Fluid Flow and Breakup Processes. *Flow Turbul. Combust.* **2024**, *112*, 615–642. [CrossRef]
17. Liu, Z.; Li, Z.; Liu, J.; Wu, J.; Yu, Y.; Ding, J. Numerical Study on Primary Breakup of Disturbed Liquid Jet Sprays Using a VOF Model and LES Method. *Processes* **2022**, *10*, 1148. [CrossRef]
18. Dekterev, A.A.; Dekterev, A.A. Method for Simplified CFD Simulation for Pressure Swirl Nozzle Atomization. *Thermophys. Aeromech.* **2024**, *31*, 1171–1176. [CrossRef]
19. Vashahi, F.; Lee, J.K. Insight into the Dynamics of Internal and External Flow Fields of the Pressure Swirl Nozzle. *At. Sprays* **2018**, *28*, 1001–1028. [CrossRef]
20. Chung, I.-P.; Presser, C. Fluid Property Effects on Sheet Disintegration of a Simplex Pressure-Swirl Atomizer. *J. Propuls. Power* **2001**, *17*, 212–216. [CrossRef]
21. Rezaei, S.; Vashahi, F.; Ryu, G.; Lee, J. On the Correlation of the Primary Breakup Length with Fuel Temperature in Pressure Swirl Nozzle. *Fuel* **2019**, *258*, 116094. [CrossRef]
22. Rostami, E.; Mahdavy Moghaddam, H. Experimental Comparison of the Spray Atomization of Heavy and Light Fuel Oil at Different Temperatures and Pressures for Pressure-Swirl Injector. *Proc. Inst. Mech. Eng. Part A J. Power Energy* **2021**, *235*, 1694–1717. [CrossRef]
23. Cai, W.; Li, W.; Zhao, Y.; Yan, Y. Experimental Research on the Influence of Aviation Fuel Temperature on Swirl Nozzle Velocity. *Fuel* **2021**, *289*, 119765. [CrossRef]
24. Ma, X.; Gao, Y.; Li, F.; Wang, S. Multi-Scale Flow Atomization Characteristics of Jatropha Biodiesel Swirl Liquid Film Breakup. *Renew. Energy* **2024**, *237*, 121670. [CrossRef]
25. Yue, Z.; Liu, H.; Gao, C.; Cheng, S.; Wang, H.; Zheng, Z.; Yao, M. A One-Way Coupling Approach for Simulating In-Nozzle Flow and Spray Characteristics of a Pressure-Swirl Atomizer. *Phys. Fluids* **2024**, *36*, 033314. [CrossRef]
26. Feng, H.; Yin, Z.; Hong, Q.; Hu, Y.; Liu, L.; Wang, J.; Huang, Q.; Zhou, Y. Atomization Characteristics of Pyrolysis Oil Derived from Waste Tires. *Waste Dispos. Sustain. Energy* **2024**, *6*, 39–52. [CrossRef]
27. Dafsari, R.A.; Lee, H.J.; Han, J.; Park, D.-C.; Lee, J. Viscosity Effect on the Pressure Swirl Atomization of an Alternative Aviation Fuel. *Fuel* **2019**, *240*, 179–191. [CrossRef]
28. Alazemi, A.A.; Alajmi, A.F.; Al-Salem, S.M. Investigation of Chemical, Physical, and Tribological Properties of Pyrolysis Oil Derived from End-of-Life Tires (ELTs) against Conventional Engine Oil. *Lubricants* **2024**, *12*, 188. [CrossRef]
29. Li, X.-G.; Fritsching, U. Process Modeling Pressure-Swirl-Gas-Atomization for Metal Powder Production. *J. Mater. Process. Technol.* **2017**, *239*, 1–17. [CrossRef]
30. Ma, X.; Wang, S.; Li, F.; Yu, X.; Jiang, S.; Wang, H. Effect of Fuel Physical Properties and Pressure on the Internal Flow Behavior of Pressure Swirl Nozzle. *Energy* **2026**, *344*, 140021. [CrossRef]
31. Harizi, W.; Hamdi, F.; Chrigui, M. A Comprehensive Numerical Investigation of the Spray Characteristics in Spill-Return Atomizers Using Coupled VOF and Euler–Lagrange Approach. *Particuology* **2024**, *95*, 319–332. [CrossRef]
32. Van Strien, J.; Petersen, P.; Lappas, P.; Yeo, L.; Rezk, A.; Vahaji, S.; Inthavong, K. Spray Characteristics from Nasal Spray Atomization. *J. Aerosol Sci.* **2022**, *165*, 106009. [CrossRef]
33. Yao, S.; Zhang, J.; Fang, T. Effect of viscosities on structure and instability of sprays from a swirl atomizer. *Exp. Therm. Fluid Sci.* **2012**, *39*, 158–166. [CrossRef]

Disclaimer/Publisher's Note: The statements, opinions and data contained in all publications are solely those of the individual author(s) and contributor(s) and not of MDPI and/or the editor(s). MDPI and/or the editor(s) disclaim responsibility for any injury to people or property resulting from any ideas, methods, instructions or products referred to in the content.